Title

Stress Effects on Vibrational Spectra of a Cubic Hybrid Perovskite: A Probe of Local Strain

Journal

The Journal of Physical Chemistry C, 124(50)

ISSN

1932-7447

Authors

Talit, Kuntal

Strubbe, David A

Publication Date

2020-12-17

DOI

10.1021/acs.jpcc.0c07389

Peer reviewed

Stress effects on vibrational spectra of cubic hybrid perovskite: A probe of local strain

Kuntal Talit[1, a] and David A. Strubbe[1, b]

[1]*Department of Physics, University of California Merced, California 95343*

(Dated: July 9, 2019)

Strain plays an important role in semiconductor performance and stability. Hybrid organic metal-halide perovskites are made in thin films and inhomogeneous residual strain may develop in the material due to thermal expansion mismatch with the substrate, polycrystallinity in the thin films or even by light soaking. These strains can affect carrier mobility, non-radiative recombination, degradation, and other optoelectronic properties. Measuring spatially varying strains is difficult but of prime importance for understanding these effects. Vibrational frequencies shift due to strain in a material, and we want to enable use of this phenomenon to map local strain within a perovskite material via Raman spectroscopy, as is done in crystalline silicon. In this work, we have used density functional theory and density functional perturbation theory to investigate the effect of applied strain on the vibrations of pseudo-cubic methylammonium lead iodide ($CH_3NH_3PbI_3$) via Raman spectroscopy. Small uniaxial strains are applied along the three cubic crystallographic directions [100], [010] and [001] to determine the frequency changes. Frequency vs strain graphs can be used as a calibration curve to probe local strain in Raman microscopy. We identify the modes most favorable for this application. We analyze the different behaviors vs. strain observed and the relation to mode characters, and structural changes under strain. We also calculate the mode Grüneisen parameters in each direction, giving information about anharmonicity within the crystal. The negative Grüneisen parameter in the c-direction implies an anisotropic negative thermal expansion in that crystal axis, as recently reported for other crystal phases.

I. INTRODUCTION

Organic-inorganic hybrid perovskites are promising materials for next generation solar cell applications.[1] They have direct bandgap[2,3], high absorption coefficient[4], long diffusion length[5,6], and large carrier mobility[7] which make them favorable for PV applications. In last 10 years the record photoconversion efficiency (PCE) has increased drastically from 3.8 %[8] to 23.7 %[9]. Owing to other benefits like ease of bandgap engineering[10,11], flexibility for use in portable electronic devices[12], tunability of transparency to light for tandem cells[13], and suitability for mass production[14] with a cheaper cost, perovskites have been the object of great interest in the solar cell industry recently. There are also other non-PV applications of perovskite, e.g. spin-optoelectronic applications[15], luminescent solar concentrators[16], and light-emitting diodes[17].

Beside these favorable properties, perovskites suffer from serious thermal or chemical instabilities[18,19] which are great hindrance to its commercial application as a solar cell. Degradation is caused by moisture[19], heat[18] and light[20]. Different encapsulation techniques can help to get rid of moisture issue[21,22] but degradation due to heat and light is still a challenge that needs to be addressed. Different studies have been reported which suggest that strain plays an important role in intrinsic stability and performance of the perovskites[23–32]. Increase in lattice strain decreases the activation energy of ion migration within the material which accelerates its degradation[25]. Residual strain within the lattice can impact the carrier dynamics and hence PCE of the device[31]. Light soaking can create small polaronic states which in presence of lattice strain and molecular orientation can create deep-level trap states and cause slow photocurrent degradation[24]. Light-induced lattice expansion can help to reduce the residual strain within the lattice and help to increase efficiency[29].

One of the best studied hybrid perovskites is methyl ammonium lead iodide (MAPI, $CH_3NH_3PbI_3$)[33,34]. Depending on temperature, it exists in three different phases: cubic (generally reported as pseudo-cubic[35]), orthorhombic and tetragonal[36]. At room temperature ($\sim$ 300 K) the crystal structure is tetragonal, and at high temperature ($\sim$ 330 K and above) the structure turns into cubic. Theoretical and experimental work has studied the bandgap, bandstructure, and effective mass[2,8,37,38] and the result suggests local symmetry breaking in the structure[39,40]. Vibrational properties of all three phases have been extensively studied[41–48]. The IR and Raman spectra of all three phases shows three distinct regimes of the vibrational frequencies, due to the Pb-I cage at low frequency, the methylammonium ion at high frequency, and coupled cage-ion modes in between[47]. There are only a few experimental results on vibrational spectroscopy available for the cubic structure[41,42,44]. Qiong Chen *et al.* has reported that it is extremely difficult to find Raman spectra for the pristine MAPI as it is very prone to degradation under the laser illumination, and that previously reported results in the low-energy regime may actually represent degradation products[49].

We have chosen for simplicity to study the high-temperature cubic phase due to its simpler structure. The cubic

phase is not only significant at high temperatures, but also it can be stabilized at lower temperature in quantum dots via ligands on the surface (for the closely related $MAPbBr_3$)[50] or use of other organic cations[51]. Due to the strong resemblance between the cubic, tetragonal, and orthorhombic phases' vibrational properties, we believe this work also gives insight into those phases.

The detailed behavior of vibrational modes under applied tensile and compressive strain for these materials has not been studied, although the macroscopic Grüneisen parameter γ, and the related thermal expansion, have been studied. For the tetragonal structure, a negative thermal expansion coefficient was found along the c-axis[52,53]. For the cubic structure, the Grüneisen parameter was reported in previous study[46,52] but only in the [100] direction. γ is a probe of anharmonicity, which is quite strong in perovskites[39], and hence relates to phonon-phonon scattering and thermal transport.

Most of the experiments done so far on perovskites has used grazing incidence X-ray diffraction (GIXRD) or normal XRD to measure the strain[25,29,31,54], or the substrate curvature method[54]. Another standard technique used to characterize perovskites and other semiconductor thin films is Raman spectroscopy,[55] which can also be used to measure the stress distribution within a material in the form of Raman microscopy. It is a well established technique for crystalline Si (c-Si) in the semiconductor industry[56], and can even be used in hydrogenated amorphous silicon, a disordered material with very broad peaks, as we showed in a previous theory-experiment collaboration[57]. By analyzing vibrations under compressive and tensile strain for cubic $CH_3NH_3PbI_3$, we have determined the calibration data needed to gauge local strain.

The paper is organized as follows. In section II we detail our methods and benchmark our structural relaxation, elastic properties, and zero strain phonon calculation, including on the simpler case of c-Si. In section III, we analyze phonon changes and structural changes, and identify the best modes for micro-Raman measurement of local strain. We also compare the Grüneisen parameter to other theory and experimental data. In section IV, we conclude.

II. METHOD

We have studied the phonon modes at q=Γ point for cubic structure of methyl ammonium lead iodide. Structural optimization and phonon mode calculations are done using density functional theory (DFT) and density functional perturbation theory (DFPT)[58] as implemented in Quantum ESPRESSO (version 6.1)[59,60]. The initial structure is taken from the work of Brivio *et al.*[46,61], with the cation oriented close to the [100] direction, which was found to be slightly favored in MD. The Brillouin zone is sampled using a half-shifted 6×6×6 Monkhorst-Pack grid with an energy cutoff of 100 Ry for the wave-functions. Atomic positions are optimized until the total force per atom is smaller than 1 meV/Å; for the initial variable-cell relaxation, a 0.5 kbar stress convergence threshold is used. The Local Density Approximation[62] (LDA) with Perdew-Wang (PW) correlation functional is used for the exchange-correlation potential in the structural optimization. Optimized Norm-Conserving Vanderbilt (ONCV) pseudopotentials[63] are used which treat Pb 5d orbitals as valence. We have not considered spin-orbit coupling as it does not have much effect on interatomic interactions at equilibrium[64]. The equilibrium structural parameters are reported in Table I. More detailed information, including results with different functionals, are reported in Table S1, along with bandgaps in Table S2 and the LDA bandstructure in Fig. S1[65].

It can be difficult to obtain an optimized exact cubic structure of MAPI without distortion to other phases[2]. Our structural optimization makes the structure pseudo-cubic, in agreement with other calculations. Optimized crystallographic angles α, β and γ are 90°, 90° and 88.8° respectively. Pb-I-Pb angles are 164.46°, 164.65° and 173.92° along a, b and c axes, respectively. The C-N bond-length is found to be 1.47 Å with average C-H and N-H bond lengths of 1.1 Å and 1.05 Å. Due to the pseudocubic lattice, off-centering of the Pb atom, cation orientation, and the octahedral tilting of the Pb-I cage, the structure has no symmetry,[35] even when we checked the structure without the $CH_3NH_3^+$ ion or with the H atoms removed. Our final cation orientation has the C-N bond lying in the xz plane, at an angle of 23.3° to the x-axis ([100] direction).

Before applying strain to the structure, convergence of the phonon frequencies, with respect to k-grid and self-consistency threshold of the phonon calculation are checked and all the strain calculations are done using self-consistency threshold 10^{-16}. Small changes in mode frequencies are noted for different functionals (PBE[67], PBESol[68] and LDA[62]). For low-frequency phonons, the pattern is (LDA>PBESol>PBE) whereas for mid (800 - 1600 cm^{-1}) and high (2900 - 3200 cm^{-1}) frequencies it is (LDA<PBESol<PBE) with most deviation at high frequencies, as shown in Fig.1. We see relatively small differences except at the highest frequencies.

For comparison, we performed similar calculations for c-Si (Fig.2) and the result follows the low frequency pattern (LDA>PBESol>PBE) as we have found in cubic MAPI. We apply uniaxial strain in the [100] direction and plot frequency changes, as the three degenerate optical phonons are split into a doublet and singlet. Results are shown in Table II and Fig. 2. LDA in fact has the best agreement with experiment for both frequency and slope, in this case; PBEsol is similar, but PBE is more different.

TABLE I: Optimized cell parameters for cubic $CH_3NH_3PbI_3$ from DFT/LDA energy minimization and comparison with previous studies using DFT/PBESol[64] and powder neutron diffraction (PND)[66] method.

	a (Å)	**b** (Å)	**c** (Å)	**d(Pb-I)** (Å)	α	β	γ
DFT/LDA	6.16	6.11	6.27	3.11	90.00	90.00	88.80
DFT/PBE	6.50	6.41	6.53	3.25	90.00	90.00	88.66
DFT/PBESol	6.29	6.25	6.38	3.17	90.00	90.00	88.64
DFT/PBESol[64]	6.29	6.23	6.37	3.17	-	-	-
PND(352 K)[66]	6.32	6.32	6.32	3.16	-	-	-

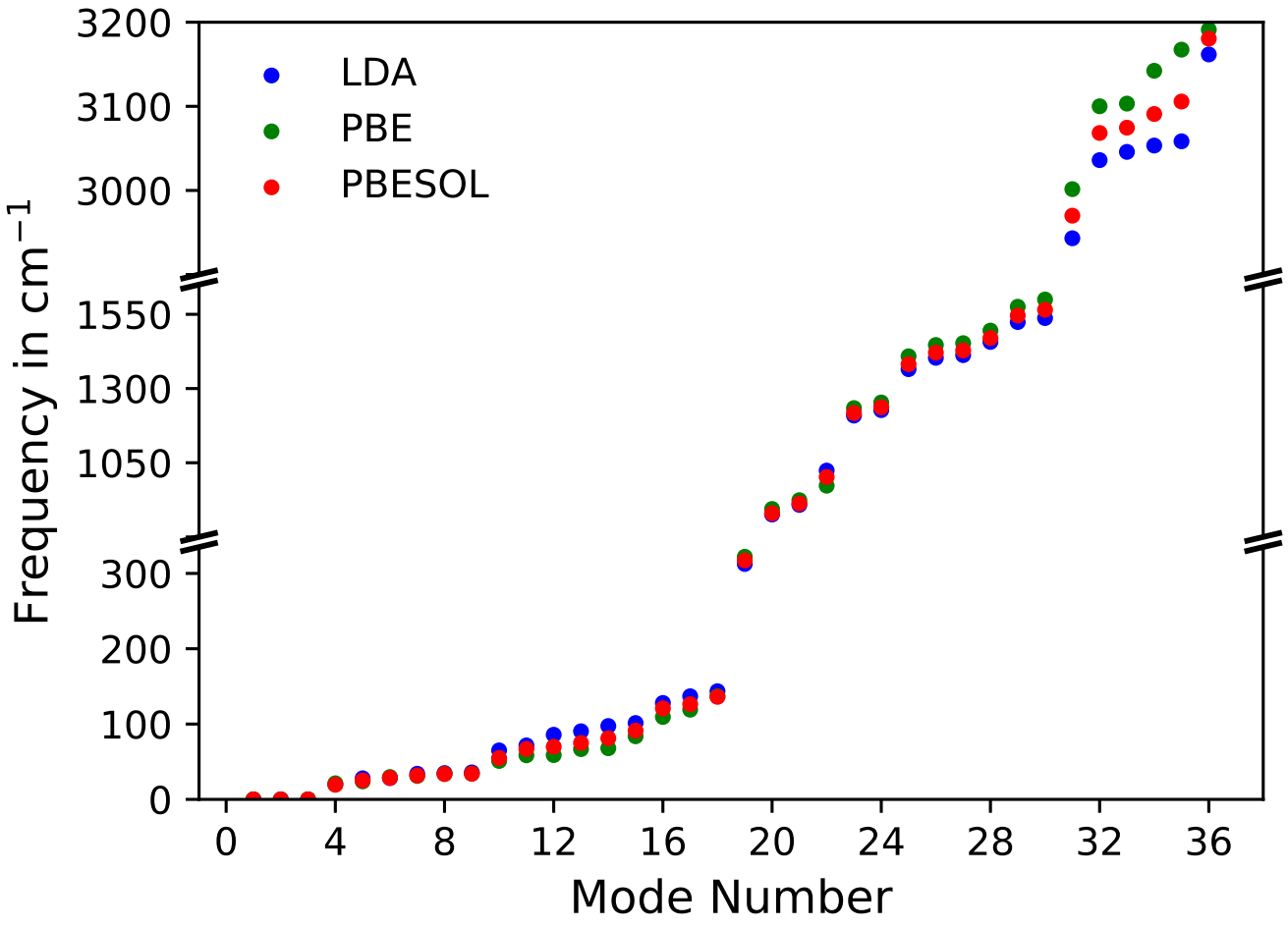

FIG. 1: Comparison of phonon frequencies with different functionals.

Moving now to the effect of strain on cubic MAPI, we applied up to 1% uniaxial compressive (negative, in our convention) and tensile (positive) strain to the optimized zero-strain structure where ϵ represents strain and a, b and c are lattice vectors. For uniaxial strain along [100] the strain operation on the lattice vectors is calculated as below:

$$\begin{pmatrix} 1 \pm \epsilon & 0 & 0 \\ 0 & 1 & 0 \\ 0 & 0 & 1 \end{pmatrix} \begin{pmatrix} a_{1x} & b_{1x} & c_{1x} \\ a_{2y} & b_{2y} & c_{2y} \\ a_{3z} & b_{3z} & c_{3z} \end{pmatrix} = \begin{pmatrix} a'_{1x} & b'_{1x} & c'_{1x} \\ a_{2y} & b_{2y} & c_{2y} \\ a_{3z} & b_{3z} & c_{3z} \end{pmatrix}$$

Similar calculations are repeated along other two crystallographic directions [010] and [001]. Note that these directions are referred to the perfect cubic structure, and therefore are the same as the Cartesian x, y, and z. We

TABLE II: Benchmark calculation of optical phonon mode frequencies at $q = 0$ for c-Si, and the split singlet and doublet slopes under uniaxial [100] strain using LDA, PBE and PBESOL. Calculated values are compared with published theoretical and experimental results. LDA has best agreement with experiment.

	ω (cm^{-1})	**singlet slope** (cm^{-1})	**doublet slope** (cm^{-1})
LDA	514	-426	-551
PBE	503	-430	-526
PBESOL	510	-422	-546
LDA[57]	514	-424	-547
Expt[69,70]	520±0.5	-481±20	-601±20

considered results up to ±0.4% of strain where the change in frequency with the applied strain falls in the linear regime for most of the modes. To make sure that this strain range is appropriate, we have also computed the elastic constants by applying isotropic, tetragonal, and trigonal strain to the cubic MAPI lattice and thereby calculating elastic constants C_{11}, C_{12} and C_{44} following the procedure in Ref. 71. Within the range of ±0.4%, our result with LDA shows good agreement with previously published results (Table III).

TABLE III: Calculated values of Young's Modulus (E), Bulk Modulus (B_v) and Shear Modulus (G_v) in GPa, and Poisson Ratio (ν) for cubic $CH_3NH_3PbI_3$.

	PBESol[72]	**PBESol+vdW**[72]	**PBE**[73]	**LDA**
E	17.20	22.80	22.20	22.53
B_v	15.60	18.50	16.40	18.96
G_v	6.50	8.70	8.70	8.66
ν	0.31	0.22	0.28	0.30

Having confirmed reasonable results for LDA on phonon frequencies and elastic constants, we are using LDA for all our strain and phonon calculations as Quantum ESPRESSO can only provide Raman intensities for LDA. Acoustic Sum Rule (ASR) with the code's ASR=crystal setting is used to make the acoustic modes exactly zero[74]. For each mode, we have calculated the mode Grüneisen parameter using the slope of the frequency versus strain graph with the formula $\gamma_i = -\frac{1}{\omega_i}\frac{d\omega_i}{d\epsilon}$[57] where ϵ is the applied strain and ω_i is the frequency of mode i. By taking the weighted average over all the modes we have calculated the Grüneisen parameter $\gamma = \frac{\Sigma_i \gamma_i C_{v,i}}{\Sigma_i C_{v,i}}$ which is correlated to the macroscopic property of the material by the relation $\gamma = \frac{\alpha K_T}{C_v \rho}$[75] where α is volume thermal expansion coefficient, K_T is isothermal bulk modulus, C_v is heat capacity at constant volume and ρ is the density. We have checked the trend of Grüneisen parameter for [100], [010] and [001] crystallographic directions.

Raman intensities are calculated using the approach of Lazzeri et al.[76] and IR intensities computed from Born effective charge tensors which are calculated as variation of macroscopic polarization with the atomic displacement using the modern theory of polarization[77]. $Z^*_{i\alpha\beta} = -\frac{\partial^2 E}{\partial d_{i\alpha}\partial \epsilon_\beta} = -\frac{\Omega}{e}\frac{\partial P_\alpha}{\partial d_{i\alpha}}$, where Ω is the volume of the unit cell, i represents a particular atom, α, β indicates Cartesian coordinates, P is the macroscopic polarization and d_i is the atomic displacement. The effective charge vector for $Z^*_{\alpha\nu}$ for a vibrational mode ν can be expressed as $Z^*_{\alpha\nu} = \sum_{i\beta} Z^*_{i\alpha\beta}\sqrt{\frac{M_o}{M_i}}\xi_{\nu i\beta}$, where M_i is the nuclear mass, M_o is the average mass over the unit cell, $\xi_{\nu i\beta}$ are the eigen modes with frequency ω_ν.

III. RESULTS

Calculated normal modes of cubic $CH_3NH_3PbI_3$ show three distinct frequency regions low (0-350 cm^{-1}) mid (850-1600 cm^{-1}) and high (2900-3200 cm^{-1}) as already noticed for cubic as well as orthorhombic and tetragonal structures in previous studies[46]. Low frequency modes are mainly contributed by the vibration of PbI_6 octahedra while the mid

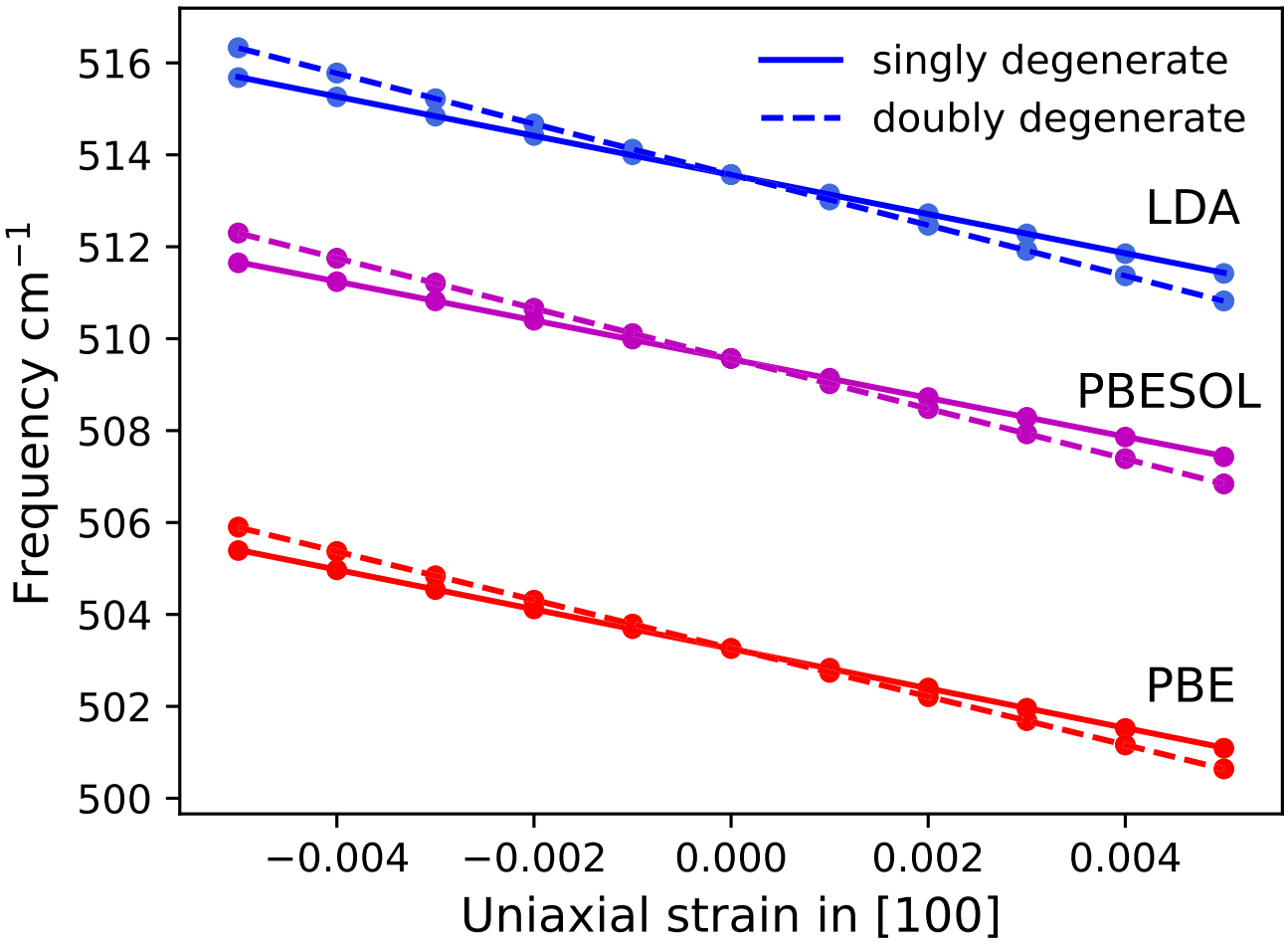

FIG. 2: Benchmark calculation of the change in optical phonon frequency of c-Si under uniaxial stress along [100], with different DFT functionals. Applied strain breaks the degeneracy of the phonon mode making a doubly degenerate (dotted) and singly degenerate (solid) mode.

and high frequency modes involve the vibration of $CH_3NH_3^+$ ion. For some of the mid-frequency modes both $CH_3NH_3^+$ ion and PbI_6 octahedra vibrations become important. Since pseudo-cubic $MAPbI_3$ does not have any symmetry, it is not possible to assign spectral activity to any particular mode using group theory. All the modes shows both IR and Raman activity to some degree, but the intensity differs and some are more IR active while some are more Raman active because of the vibrational nature of the $CH_3NH_3^+$ ion and PbI_6 octahedra.

Our *ab initio* IR and Raman results are shown in Fig. 3. Our Γ-point phonon modes are convolved with 1 cm^{-1} Lorentzian broadening and compared with the calculations of F. Brivio *et al.*[46]. The difference in results are due to use of different functionals and methods. They have used PBESol and we used LDA, and this difference is expected as we have seen from our analysis at Fig. 1. Calculated Raman and IR frequencies match well with published theoretical and experimental results[41,42,44,46]. Most experimental results are available only in the low frequency region.

We have studied how structural parameters change with applied strain. For applied strain along [100], we noticed that the change in bond length is linear in this range of applied strain. The Pb-Pb distance is smaller than the sum of the Pb-I and I-Pb bond length which indicates that Pb-I-Pb bond angle changed with applied strain: it decreases along a and increases in b and c. Fig4 shows the change in Pb-I bond length and Pb-I-Pb bond angle for uniaxial strain along [100]. There are almost no changes in the C-N bond length which suggest that the uniaxial strain does not create any deformation in the ion. However, it does rotate, with an increasing angle under compressive strain and a decreasing angle under tensile strain, with changes of up to 1.5° over our strain range. Rotation is largest for [001] strain. Full plots of structural parameters with each direction of strain are in Fig. S2, and all atomic coordinates of relaxed strained structures.[65]

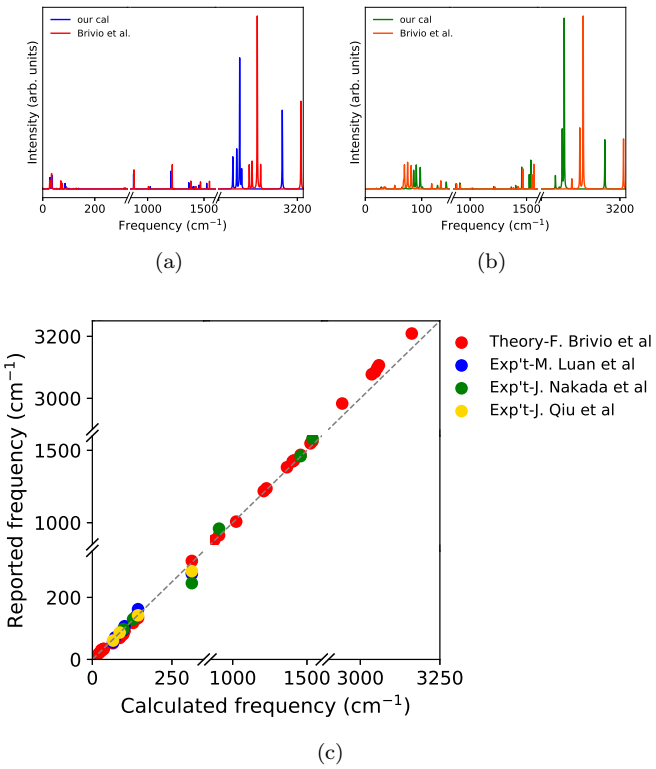

FIG. 3: Comparison of calculated Raman and IR frequencies. (a) Comparison of Raman frequencies convolved with 1 cm^{-1} Lorentzian broadening with calculation of F. Brivio *et al.*[46] (b) Similar comparison for IR frequencies. (c) Comparison of Raman and IR frequencies with published theoretical and experimental results.

We have 12 atoms in our unit cell for cubic $CH_3NH_3PbI_3$ which gives 36 phonon modes, of which 3 have exactly zero frequency according to the ASR. For the other 33 modes we plotted frequency vs. applied strain (both compressive and tensile). Different patterns of frequency vs. applied strain are noticed for different modes. Some of them are linear, some are parabolic, and some are neither. For comparison, c-Si shows linear changes for small strain, and a splitting of degeneracy, as we have seen. Given the much more complicated structure of the perovskite and lack of symmetry, more complex behavior is observed. Only a few low-frequency modes which are nearly degenerate in frequency show the parabolic pattern. The modes which approach or cross under strain are shown in Fig. 7. Using the eigenvectors as a guide, in a few cases, we found crossing of modes under strain, and therefore relabeled the modes to maintain character. The parabolic behavior is due to gradual strain-induced mixing between the modes, and can be analyzed by nearly degenerate perturbation theory. Other modes with irregular behavior show even more mixing between modes, in a non-perturbative way, which we attribute to strong coupling to structural changes. The other modes where the frequency change is mostly linear can be categorized into three different types. i) slope of [100] and [010] strain are similar while the slope of [001] strain are different. ii) slope of [100] and [001] strain are exactly same and [010] strain is different. iii) slope of [100] and [001] strain are exactly same for tensile strain and slope of [010] and [001] strain are same for compressive strain. These behaviors indicate approximate symmetries of particular modes. In Fig.5, we provide four representative modes' frequency vs. strain.

To understand this behavior, we plotted eigenvectors (displacement patterns) for each mode; those for the chosen four representative modes are given in Fig. 6. Corresponding plots for all modes are given in Fig. S3[65]. Fig5(a) shows a kink at zero for the frequency for both [010] and [001] directional strain while for [100] strain it is almost linear. The mode eigenvectors also shows similar trend for [010] (Fig. 6(a)) and [001] directions, indicating a symmetry along these two directions for this kind of modes. The mode's character is a combination of translation of the $CH_3NH_3^+$ ion and a Pb-I-Pb rocking mode. Fig5(b) shows parabolic frequency changes for [100] and [010] strain. Mode eigenvectors for this mode at [100] (Fig. 6(b)) and [010] also shows parabolic nature while for [001] direction it is linear but with a step. This mode is a combination of $CH_3NH_3^+$ ion libration and a Pb-I-Pb rocking mode. Fig5(c) shows all linear frequency changes where uniaxial strain along [100] and [001] makes exactly the same shift. Mode eigenvectors shows a linear pattern (Fig. 6(c))) with small slopes, indicating a lack of mixing, hence like the non-degenerate perturbation theory case which will in general give a linear change. The mode character is libration with spin for $CH_3NH_3^+$ ion

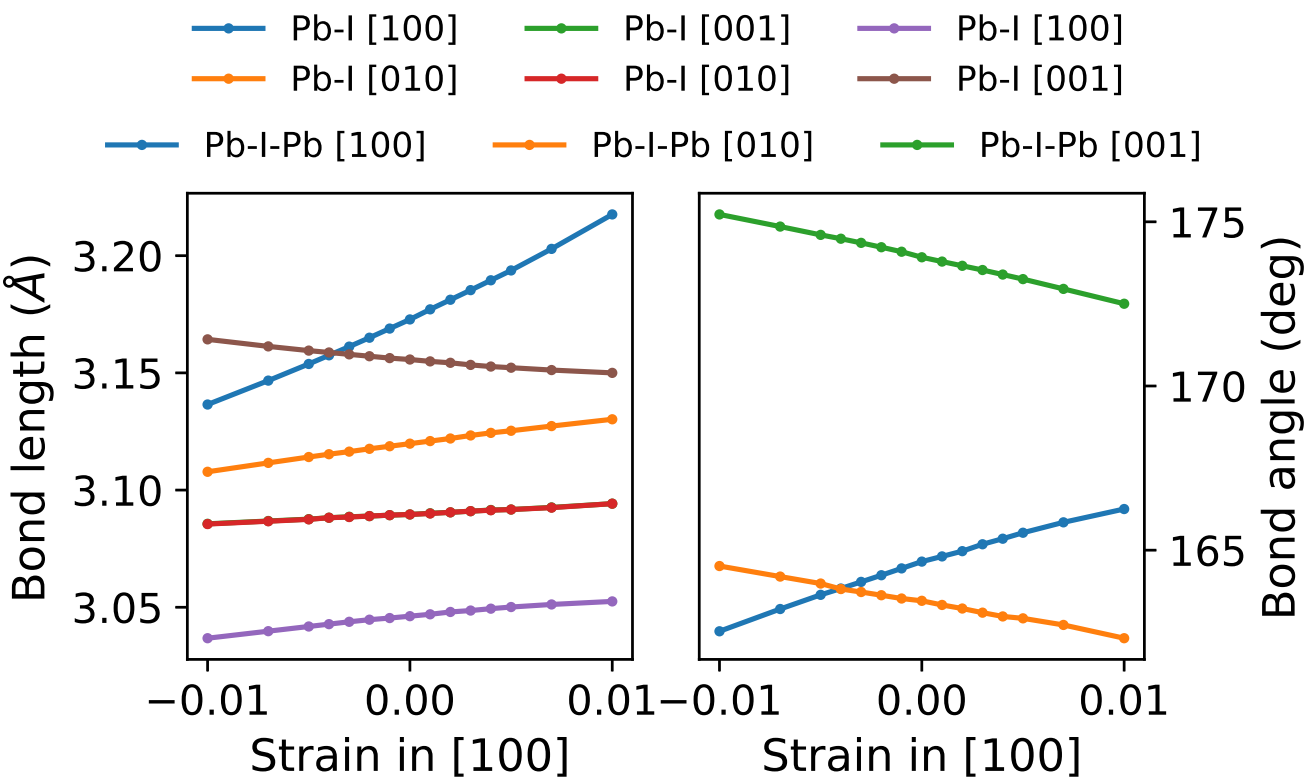

FIG. 4: Change in Pb-I bond length and Pb-I-Pb bond angle in cubic $CH_3NH_3PbI_3$ for uniaxial [100] strain, showing fairly linear relationships, and a buckling of the Pb-I cage.

and Pb-I-Pb bending. Fig5(d) shows a frequency change pattern which is neither linear nor parabolic, although the eigenvector change pattern for this mode along all three directions are linear, surprisingly (Fig. 6(d)). This is a pure molecular mode with symmetric C-H and N-H bending with C-N stretch, which must somehow be coupling to nonlinear changes in interatomic force constants.

From our full phonon analysis, shown in Table S3,[65] we found that parabolic modes are generally more Raman-active and less IR-active. Modes that have all positive or all negative slopes along all three directions have an IR intensity vector lying in the plane. Modes which have high slopes in all three directions – among them, high frequency modes (3053.38 cm^{-1}, 3058.42 cm^{-1}, 3161.71 cm^{-1}) – are both highly IR- and Raman-active while low frequency modes(27.97 cm^{-1}, 65.02 cm^{-1}, 85.82 cm^{-1}) are less IR- and Raman-active. Libration and translation of $CH_3NH_3^+$ ion and Pb-I-Pb vibration are responsible for high slopes along [100] direction while modes having high slope in [010] shows C-H and N-H stretch in $CH_3NH_3^+$ ion.

Given that cations rotate at room temperature, we need to check the robustness of our frequencies with respect to cation rotation. Phonon calculations are not very meaningful except from a relaxed structure, and only a few cation orientations are stable. We took our zero-strain structure and rotated the cation to the [111] direction and relaxed, which ended with the cation in the xz plane, with the C-N bond at angle of 113.9° (compared to 23.3° for our main data set). From a phonon calculation, we find some frequency changes due to the $CH_3NH_3^+$ rotation, typically by a few wavenumbers. Full results are shown in Table S3.[65]

After this analysis, we can identify the best modes for IR or Raman microscopy for probing local strain. An appropriate mode should have a large IR or Raman intensity, for ease of detection; a linear frequency change with strain, for simple and unique relation of frequency to strain; a large slope for frequency vs. strain, for sufficient signal-to-noise ratio in measuring frequency shifts; and finally a small change in frequency with respect to cation orientation, ensuring the validity of our results in the presence of cation rotations at elevated temperature[35]. We note 5 suitable modes, whose properties are detailed in Table IV and displacement patterns are shown in Fig. 8. The frequency changes vs. strain are shown in Fig. 9 and the eigenvectors vs. strain are shown in Fig. 10, exhibiting little change in mode character. Each of these modes has all slopes positive or all slopes negative. This is convenient because it means that in the case of triaxial strain or when cation rotations wash out directional dependence, when

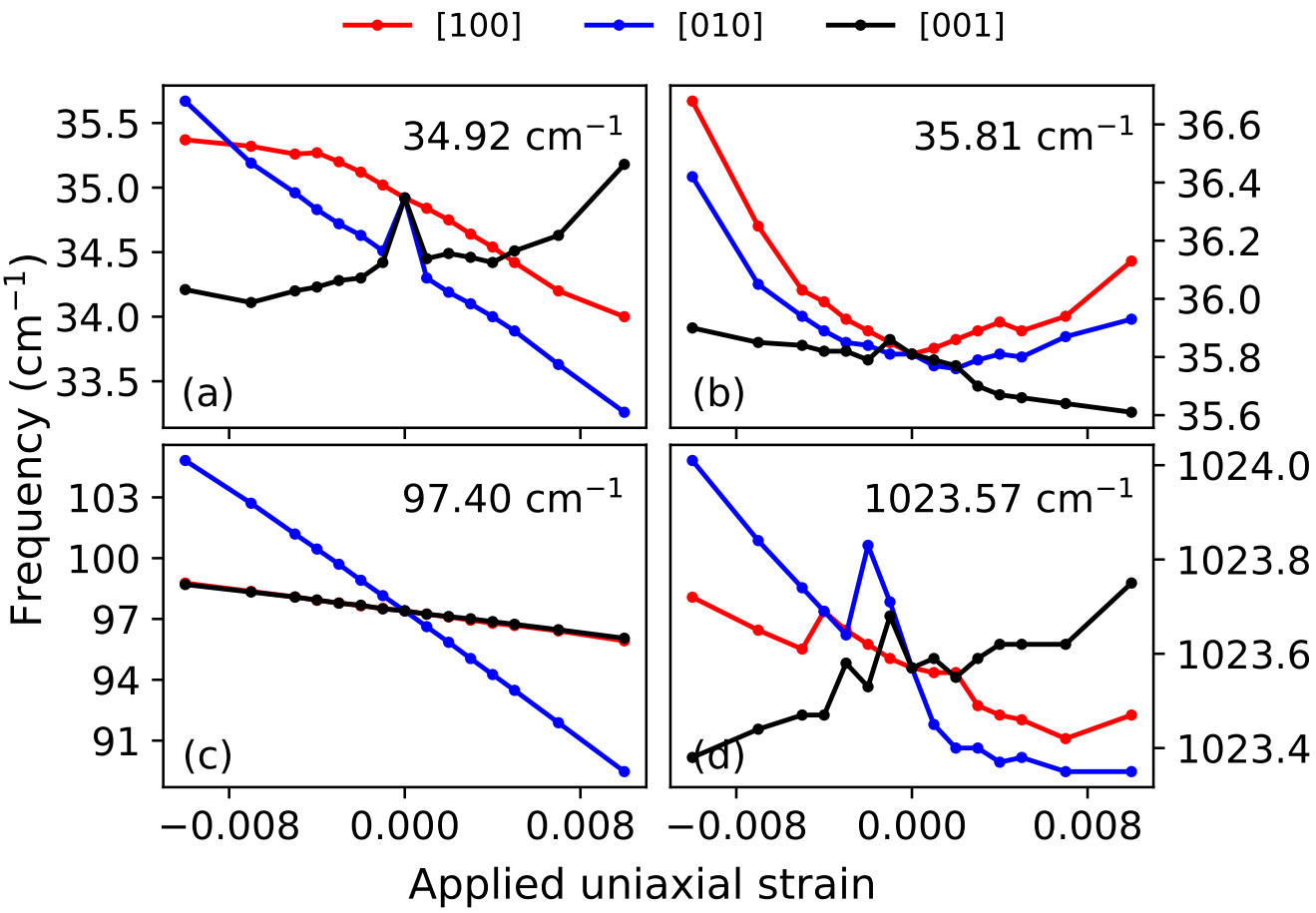

FIG. 5: Frequency changes with applied compressive and tensile strain in three crystallographic directions [100], [010] and [001]. (a) Deep kink at zero strain for [010] and [001] but otherwise almost linear. (b) Parabolic pattern for [100] and [010] uniaxial strain. (c) Linear pattern. (d) Erratic pattern is neither linear nor parabolic.

the average of the three uniaxial slopes would be the appropriate slope, the three directions will reinforce each other rather than cancelling out as could happen when the slopes have different signs.

The mode Grüneisen parameter is calculated using the slope of the frequency vs strain curve for each mode (Fig. 11), as done in a-Si[57]. Pb-I vibrations at lower frequency have significant values, whereas $CH_3NH_3^+$ ion vibrations at higher frequency have much smaller values. One of the reasons for the low values at high frequency is the high frequency itself, as we divide the slope with the mode frequency, although some high-frequency modes do have large absolute slopes. To connect to macroscopic properties, we calculate the Grüneisen parameter, as the weighted average over all the modes using the Bose-Einstein formula for heat capacity. In distinction to F. Brivio *et al.*, we are using uniaxial strain, and we include only modes at $q = \Gamma$, because of the conceptual problem in the quasiharmonic approximation of how to handle the imaginary frequencies.[78] They occur around q=R and q=M, and are not reduced by strain (Table S4[65]). The imaginary frequencies are indicative of the fact that the cubic structure is not the most stable phase at $T = 0$, and were observed in previous work[46]. Our calculated values of the directional Grüneisen parameter at 330 K for strain along [100], [010], and [001] are 1.06, 2.10, and -0.51, respectively, for an average of 0.88. The isotropic value reported by F. Brivio *et al.*[46], averaged over temperature, was 1.6. This result shows a directional dependency of the Grüneisen parameter that suggests negative thermal expansion along [001] direction for cubic MAPI, due to the negative value. Similar results were noticed in the case of tetragonal perovskites for negative thermal expansion coefficient along the c-axis[79,80].

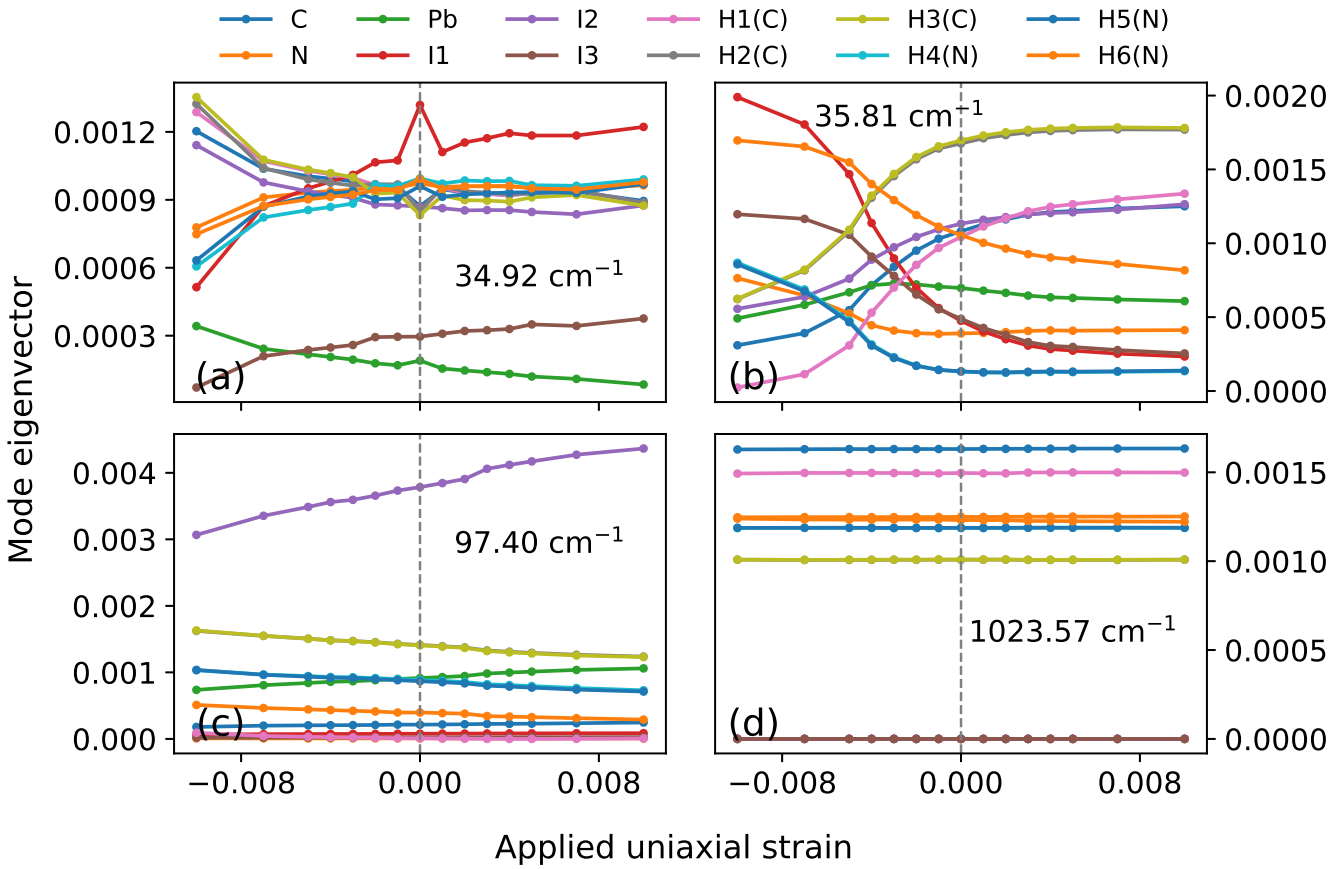

FIG. 6: Mode eigenvectors for the representative modes presented in Fig. 5. Uniaxial strains are in the (a) [010], (b) [100], (c) [001], and (d) [001] directions, showing connections between parabolic or other nonlinear frequency behavior in (a) and (b) with significant changes in mode character, while (c) has little character change and linear frequency behavior, and (d) anomalously has little character change but erratic frequency behavior.

IV. CONCLUSION

We have comprehensively studied the structural and vibrational properties of cubic $CH_3NH_3PbI_3$ under uniaxial strain. We find that not only the Pb-I bond lengths but also the Pb-I-Pb bond angles change under strain, showing a buckling of the Pb-I lattice. The cation remains undistorted but rotates with respect to the lattice. The phonon modes have frequency changes under strain, which can have linear, parabolic, or irregular patterns. Linear is associated with no change in mode character with strain, while parabolic is associated with small changes and irregular patterns with large changes in mode character, as modes mix. These changes give insight into the interplay between structure, strain, and vibrations, and show approximate symmetries for some modes. We have identified 5 modes that are promising for IR or Raman microscopy measurement of local strain, as done in other semiconductors and even amorphous Si which has broad peaks. Results on the mode Grüneisen parameters and macroscopic Grüneisen parameters give insight into anharmonicity and directional negative thermal expansion. Our study of the cubic phase is relevant not only to high temperatures but also to cubic phases stabilized by ligands or other cations, and is expected to be similar in many respects to results for the tetragonal and orthorhombic phases at lower temperature.

Acknowledgments

We acknowledge a helpful discussion with Yong Zhang. Work was supported by UC Merced start-up funds and the Merced nAnomaterials Center for Energy and Sensing (MACES), a NASA-funded research and education center, under award NNX15AQ01. This work used computational resources from the Multi-Environment Computer for Exploration and Discovery (MERCED) cluster at UC Merced, funded by National Science Foundation Grant No. ACI-1429783,

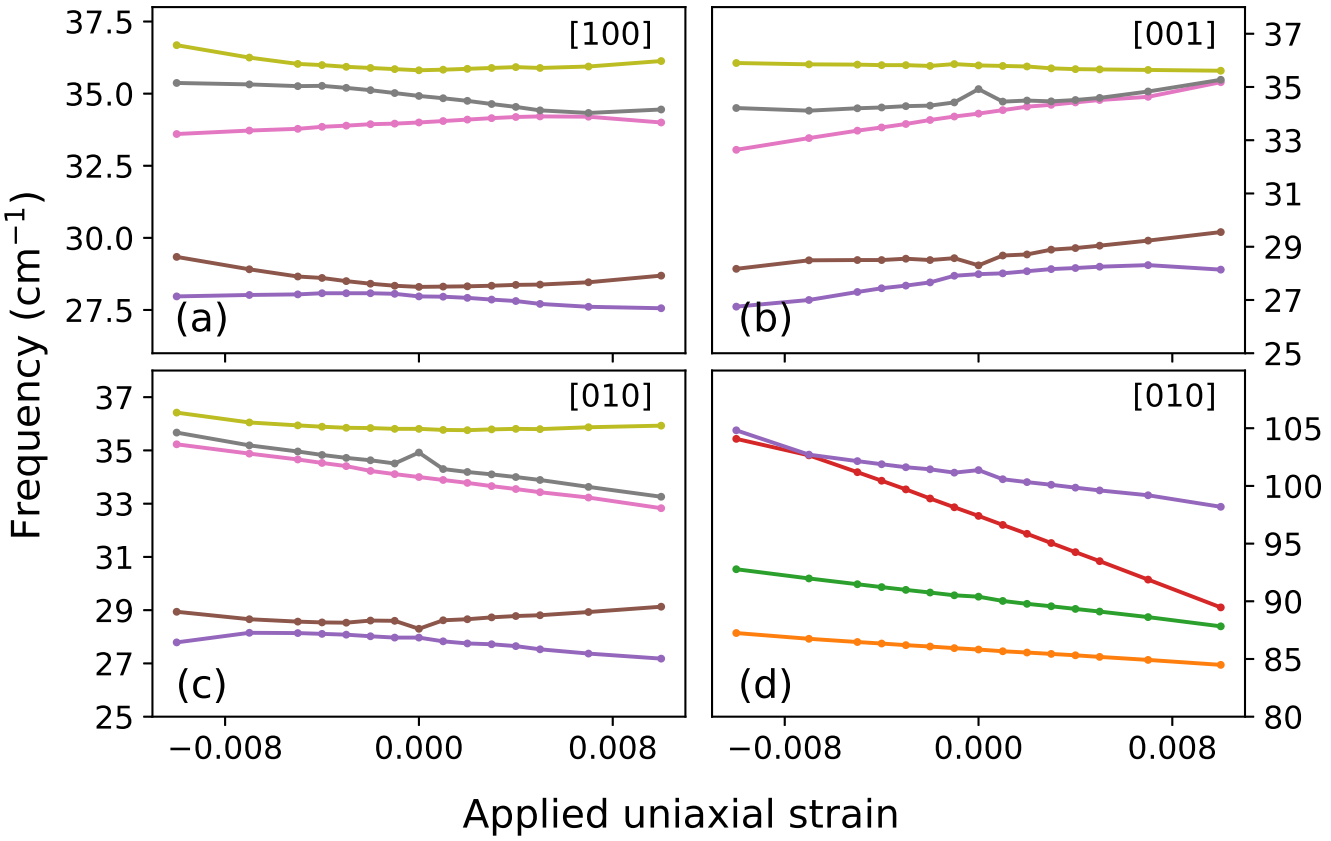

FIG. 7: Frequencies of modes which approach or cross under strain, giving rise to parabolic or irregular behavior in frequency vs. strain.

and the National Energy Research Scientific Computing Center (NERSC), a U.S. Department of Energy Office of Science User Facility operated under Contract No. DE-AC02-05CH11231.

---

[a] Electronic address: ktalit@ucmerced.edu
[b] Electronic address: dstrubbe@ucmerced.edu

[1] M. A. Green, A. Ho-Baillie, and H. J. Snaith, Nat. Photon. **8**, 506 (2014).
[2] K. Frohna, T. Deshpande, J. Harter, W. Peng, B. A. Barker, J. B. Neaton, S. G. Louie, O. M. Bakr, D. Hsieh, and M. Bernardi, Nat. Commun. **9**, 1829 (2018).
[3] P. Umari, E. Mosconi, and F. De Angelis, Scientific reports **4**, 4467 (2014).
[4] M. Shirayama, H. Kadowaki, T. Miyadera, T. Sugita, M. Tamakoshi, M. Kato, T. Fujiseki, D. Murata, S. Hara, T. N. Murakami, et al., Phys. Rev. Appl. **5**, 014012 (2016).
[5] S. D. Stranks, G. E. Eperon, G. Grancini, C. Menelaou, M. J. P. Alcocer, T. Leijtens, L. M. Herz, A. Petrozza, and H. J. Snaith, Science **342**, 341 (2013).
[6] G. Xing, N. Mathews, S. Sun, S. S. Lim, Y. M. Lam, M. Grätzel, S. Mhaisalkar, and T. C. Sum, Science **342**, 344 (2013).
[7] C. Wehrenfennig, G. E. Eperon, M. B. Johnston, H. J. Snaith, and L. M. Herz, Advanced materials (Deerfield Beach, Fla.) **26**, 1584 (2014).
[8] A. Kojima, K. Teshima, Y. Shirai, and T. Miyasaka, Journal of the American Chemical Society **131**, 6050 (2009).
[9] https://www.nrel.gov/pv/assets/pdfs/pv-efficiency-chart.20181221.pdf.
[10] G. E. Eperon, T. Leijtens, K. A. Bush, R. Prasanna, T. Green, J. T.-W. Wang, D. P. McMeekin, G. Volonakis, R. L. Milot, R. May, et al., Science **354**, 861 (2016).
[11] Q. Lin, A. Armin, R. C. R. Nagiri, P. L. Burn, and P. Meredith, Nature Photonics **9**, 106 (2015).
[12] D. Yang, R. Yang, S. Priya, and S. F. Liu, Angewandte Chemie International Edition **58**, 4466 (2019).
[13] C. D. Bailie, M. G. Christoforo, J. P. Mailoa, A. R. Bowring, E. L. Unger, W. H. Nguyen, J. Burschka, N. Pellet, J. Z. Lee, M. Grätzel, et al., Energy & Environmental Science **8**, 956 (2015).

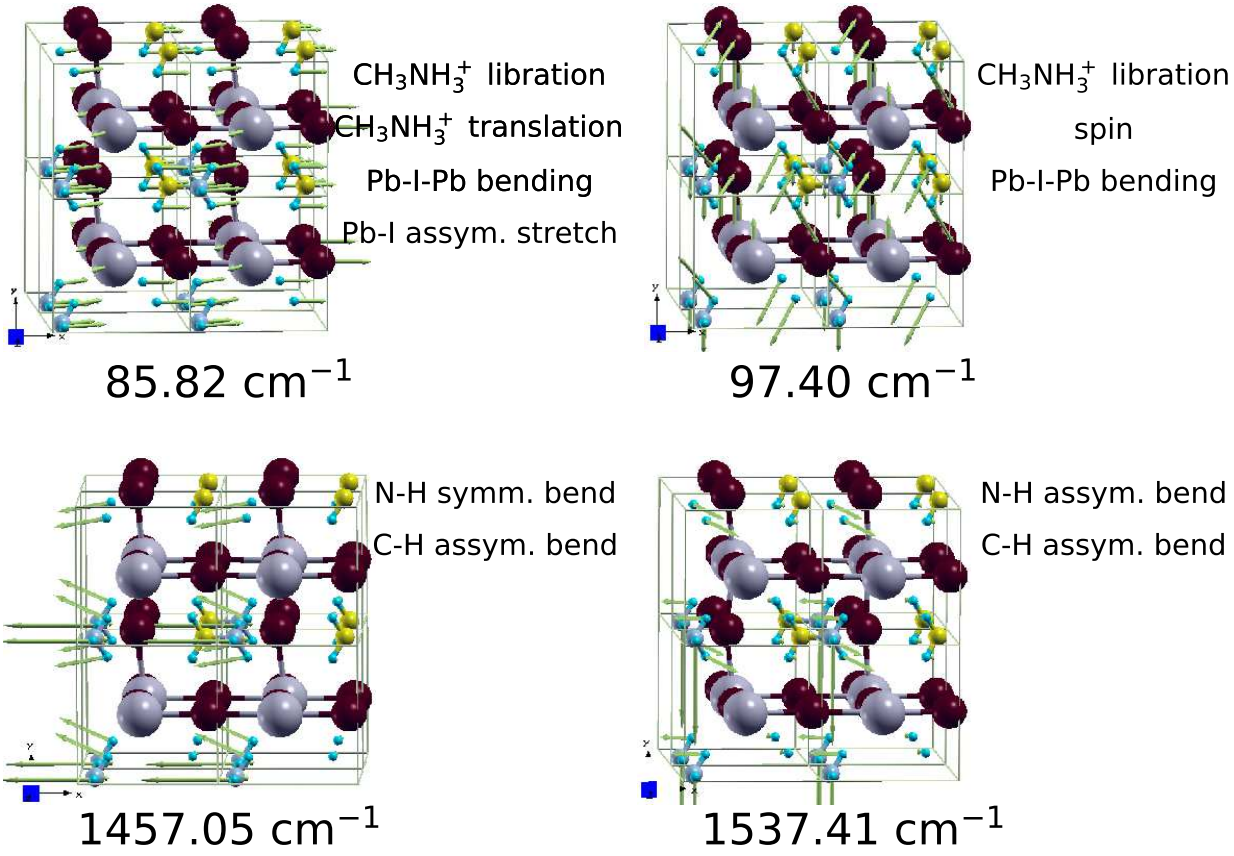

FIG. 8: Mode characters of best modes for IR/Raman microscopy to probe local strain.

[14] C. Roldán-Carmona, O. Malinkiewicz, A. Soriano, G. M. Espallargas, A. Garcia, P. Reinecke, T. Kroyer, M. I. Dar, M. K. Nazeeruddin, and H. J. Bolink, Energy & Environmental Science **7**, 994 (2014).
[15] Y. Ping and J. Z. Zhang, J. Phys. Chem. Lett. **9**, 6103 (2018).
[16] K. Nikolaidou, S. Sarang, C. Hoffman, B. Mendewala, H. Ishihara, J. Q. Lu, B. Ilan, V. Tung, and S. Ghosh, Advanced Optical Materials **4**, 2126 (2016).
[17] H. Kim, L. Zhao, J. S. Price, A. J. Grede, K. Roh, A. N. Brigeman, M. Lopez, B. P. Rand, and N. C. Giebink, Nat. Commun. **9**, 4893 (2018).
[18] B. Conings, J. Drijkoningen, N. Gauquelin, A. Babayigit, J. D'Haen, L. D'Olieslaeger, A. Ethirajan, J. Verbeeck, J. Manca, E. Mosconi, et al., Advanced Energy Materials **5**, 1500477 (2015).
[19] G. Niu, X. Guo, and L. Wang, Journal of Materials Chemistry A **3**, 8970 (2015).
[20] P. H. Joshi, L. Zhang, I. M. Hossain, H. A. Abbas, R. Kottokkaran, S. P. Nehra, M. Dhaka, M. Noack, and V. L. Dalal, AIP Advances **6**, 115114 (2016).
[21] J.-W. Lee, D.-H. Kim, H.-S. Kim, S.-W. Seo, S. M. Cho, and N.-G. Park, Advanced Energy Materials **5**, 1501310 (2015).
[22] X. Li, M. Tschumi, H. Han, S. S. Babkair, R. A. Alzubaydi, A. A. Ansari, S. S. Habib, M. K. Nazeeruddin, S. M. Zakeeruddin, and M. Grätzel, Energy Technology **3**, 551 (2015).
[23] K. P. Ong, T. W. Goh, Q. Xu, and A. Huan, J. Phys. Chem. A **119**, 11033 (2015).
[24] W. Nie, J. C. Blancon, A. J. Neukirch, K. Appavoo, H. Tsai, M. Chhowalla, M. A. Alam, M. Y. Sfeir, C. Katan, J. Even, et al., Nat. Commun. **7**, 1 (2016).
[25] J. Zhao, Y. Deng, H. Wei, X. Zheng, Z. Yu, Y. Shao, J. E. Shield, and J. Huang, Sci. Adv. **3**, 3 (2017).
[26] M. Faghihnasiri, M. Izadifard, and M. E. Ghazi, J. Phys. Chem. C **121**, 27059 (2017).
[27] L. Zhang, W. Geng, C.-j. Tong, X. Chen, T. Cao, and M. Chen, Scientific reports **8**, 7760 (2018).
[28] J. S. Bechtel and A. Van der Ven, Phys. Rev. Mater. **2**, 025401 (2018).
[29] H. Tsai, R. Asadpour, J.-C. Blancon, C. C. Stoumpos, O. Durand, J. W. Strzalka, B. Chen, R. Verduzco, P. M. Ajayan, S. Tretiak, et al., Science **360**, 67 (2018).
[30] T. W. Jones, A. Osherov, M. Alsari, M. Sponseller, B. C. Duck, Y.-K. Jung, C. Settens, F. Niroui, R. Brenes, C. V. Stan, et al., Energy & Environmental Science **12**, 596 (2019).
[31] C. Zhu, X. Niu, Y. Fu, N. Li, C. Hu, Y. Chen, X. He, G. Na, P. Liu, H. Zai, et al., Nat. Commun. **10** (2019).

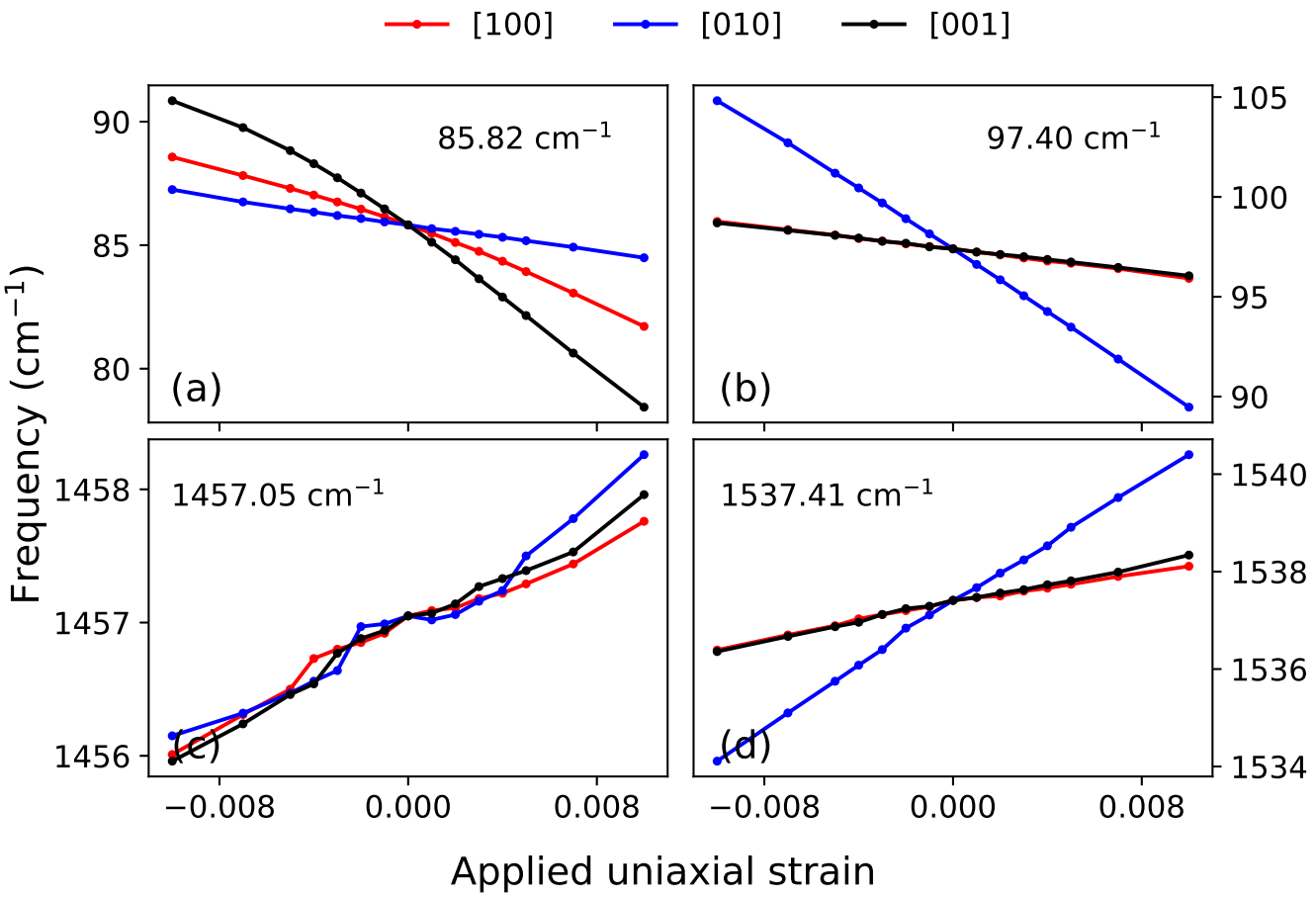

FIG. 9: Frequency vs. strain for the best modes for IR/Raman microscopy to probe local strain, showing linear changes for robust calibration.

[32] D. J. Slotcavage, H. I. Karunadasa, and M. D. McGehee, ACS Energy Letters **1**, 1199 (2016).
[33] J. Huang, Y. Yuan, Y. Shao, and Y. Yan, Nat. Rev. Mater. **2**, 17042 (2017).
[34] A. K. Jena, A. Kulkarni, and T. Miyasaka, Chemical reviews **119**, 3036 (2019).
[35] J. Even, J. Phys. Chem. Lett. **6**, 2238 (2015).
[36] T. Baikie, Y. Fang, J. M. Kadro, M. Schreyer, F. Wei, S. G. Mhaisalkar, M. Graetzel, and T. J. White, J. Mater. Chem. A **1**, 5628 (2013).
[37] G. Giorgi, J.-i. I. Fujisawa, H. Segawa, and K. Yamashita, J. Phys. Chem. Lett. **4**, 4213 (2013).
[38] M. R. Filip, C. Verdi, and F. Giustino, J. Phys. Chem. C **119**, 25209 (2015).
[39] L. D. Whalley, J. M. Frost, Y.-K. Jung, and A. Walsh, J. Chem. Phys **146**, 220901 (2017).
[40] S. McKechnie, J. M. Frost, D. Pashov, P. Azarhoosh, A. Walsh, and M. Van Schilfgaarde, Phys. Rev. B **98**, 085108 (2018).
[41] M. Luan, J. Song, X. Wei, F. Chen, and J. Liu, CrystEngComm **18**, 5257 (2016).
[42] J. Qiu, L. L. McDowell, and Z. Shi, Crystal Growth & Design (2019).
[43] M. Ledinský, P. Löper, B. Niesen, J. Holovský, S.-J. Moon, J.-H. Yum, S. De Wolf, A. Fejfar, and C. Ballif, J. Phys. Chem. Lett. **6**, 401 (2015).
[44] K. Nakada, Y. Matsumoto, Y. Shimoi, K. Yamada, and Y. Furukawa, Molecules **24**, 626 (2019).
[45] M. A. Pérez-Osorio, Q. Lin, R. T. Phillips, R. L. Milot, L. M. Herz, M. B. Johnston, and F. Giustino, J. Phys. Chem. C **122**, 21703 (2018).
[46] F. Brivio, J. M. Frost, J. M. Skelton, A. J. Jackson, O. J. Weber, M. T. Weller, A. R. Goñi, A. M. A. Leguy, P. R. F. Barnes, and A. Walsh, Phys. Rev. B **92**, 144308 (2015).
[47] M. A. Pérez-Osorio, R. L. Milot, M. R. Filip, J. B. Patel, L. M. Herz, M. B. Johnston, and F. Giustino, J. Phys. Chem. C **119**, 25703 (2015).
[48] T. Glaser, C. Müller, M. Sendner, C. Krekeler, O. E. Semonin, T. D. Hull, O. Yaffe, J. S. Owen, W. Kowalsky, A. Pucci, et al., J. Phys. Chem. Lett. **6**, 2913 (2015).
[49] Q. Chen, H. Liu, H.-S. Kim, Y. Liu, M. Yang, N. Yue, G. Ren, K. Zhu, S. Liu, N.-G. Park, et al., Phys. Rev. X **6**, 031042 (2016).

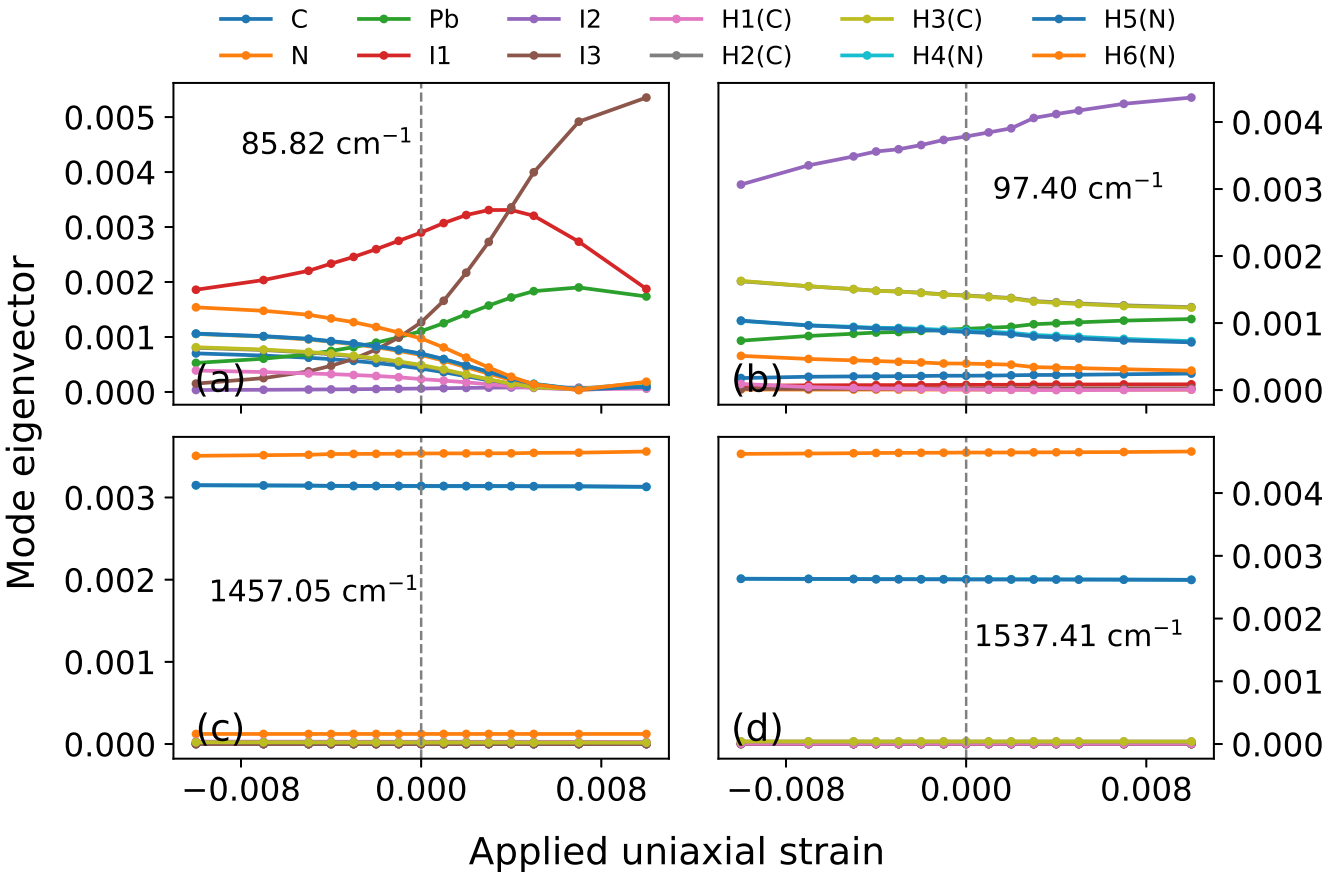

FIG. 10: Mode eigenvector vs. strain for the best modes for IR/Raman microscopy to probe local strain, showing little change in mode character (except for (a)), associated with robust linear changes vs. strain.

[50] S. Sarang, S. Bonabi Naghadeh, B. Luo, P. Kumar, E. Betady, V. Tung, M. Scheibner, J. Z. Zhang, and S. Ghosh, J. Phys. Chem. Lett. **8**, 5378 (2017).
[51] C. Wu, K. Chen, D. Guo, S. Wang, and P. Li, RSC Advances **8**, 2900 (2018).
[52] C. Ge, M. Hu, P. Wu, Q. Tan, Z. Chen, Y. Wang, J. Shi, and J. Feng, J. Phys. Chem. C **122**, 15973 (2018).
[53] R. Heiderhoff, T. Haeger, N. Pourdavoud, T. Hu, M. Al-Khafaji, A. Mayer, Y. Chen, H.-C. Scheer, and T. Riedl, J. Phys. Chem. C **121**, 28306 (2017).
[54] N. Rolston, K. A. Bush, A. D. Printz, A. Gold-Parker, Y. Ding, M. F. Toney, M. D. McGehee, and R. H. Dauskardt, Advanced Energy Materials **8**, 1802139 (2018).
[55] P. Pistor, A. Ruiz, A. Cabot, and V. Izquierdo-Roca, Sci. Rep. **6**, 35973 (2016).
[56] I. De Wolf, Semiconductor science and technology **11**, 139 (1996).
[57] D. A. Strubbe, E. C. Johlin, T. R. Kirkpatrick, T. Buonassisi, and J. C. Grossman, Phys. Rev. B **92**, 241202(R) (2015).
[58] S. Baroni, S. de Gironcoli, A. Dal Corso, and P. Giannozzi, Rev. Mod. Phys. **73**, 515 (2001).
[59] P. Giannozzi, S. Baroni, N. Bonini, M. Calandra, R. Car, C. Cavazzoni, D. Ceresoli, G. L. Chiarotti, M. Cococcioni, I. Dabo, et al., J. Phys. Condens. Matter. **21**, 395502 (2009).
[60] `http://www.quantum-espresso.org`.
[61] `https://github.com/WMD-group/hybrid-perovskites/blob/master/2015_ch3nh3pbi3_phonons_PBEsol/CH3NH3PbI3_cubic.cif`.
[62] J. P. Perdew and A. Zunger, Phys. Rev. B **23**, 5048 (1981).
[63] D. R. Hamann, Phys. Rev. B **88**, 085117 (2013).
[64] F. Brivio, J. M. Frost, J. M. Skelton, A. J. Jackson, O. J. Weber, M. T. Weller, A. R. Goni, A. M. A. Leguy, P. R. F. Barnes, and A. Walsh, Phys. Rev. B **92**, 144308 (2015).
[65] See Supplemental Material at [URL will be inserted by publisher] for more details on structural parameters, bandstructure and bandgap, phonon mode characterization, structural changes with strain, mode eigenvector and frequency changes with strain, and imaginary modes at the q=M and q=R points. Also all relaxed atomic coordinates used in this work are provided.
[66] M. T. Weller, O. J. Weber, P. F. Henry, A. M. Di Pumpo, and T. C. Hansen, Chem. Commun. **51**, 4180 (2015).
[67] J. P. Perdew, K. Burke, and M. Ernzerhof, Phys. Rev. Lett. **77**, 3865 (1996).
[68] J. P. Perdew, A. Ruzsinszky, G. I. Csonka, O. A. Vydrov, G. E. Scuseria, L. A. Constantin, X. Zhou, and K. Burke, Phys.

TABLE IV: Best modes for IR or Raman microscopy to probe local strain. Absolute IR intensity is in $(D/A)^2$/amu units and Raman intensity in A^4/amu units as per the Quantum ESPRESSO standard output. These modes are either all positive or all negative along all three crystallographic directions.

Freq (cm^{-1})	**IR Intensity**	**Raman Intensity**	**slope [100]**	**slope [010]**	**slope [001]**	**mode character**
85.8	4.77	193.2	-334.8	-127.8	-677.0	$CH_3NH_3^+$ libration $CH_3NH_3^+$ translation Pb-I-Pb bending Pb-I assym. stretch
97.4	5.53	20.2	-140.8	-772.7	-132.8	$CH_3NH_3^+$ libration, spin Pb-I-Pb bending
1365.3	0.53	222.7	85.7	84	34.8	C-N stretch C-H symm. bending no Pb-I-Pb vibration
1457.1	5.65	138.9	63.2	74.8	88.5	C-N stretch N-H symm. bending C-H assym. bending no Pb-I-Pb vibration
1537.4	7.48	15.6	79.2	302.3	90.5	C-H, N-H assym. bending no Pb-I-Pb vibration

Rev. Lett. **100**, 136406 (2008).

[69] J. Parker Jr, D. Feldman, and M. Ashkin, Phys. Rev. **155**, 712 (1967).

[70] E. Anastassakis, A. Cantarero, and M. Cardona, Phys. Rev. B **41**, 7529 (1990).

[71] F. Giustino, *Materials modelling using density functional theory: properties and predictions* (Oxford University Press, 2014).

[72] M. Faghihnasiri, M. Izadifard, and M. E. Ghazi, J. Phys. Chem. C **121**, 27059 (2017).

[73] J. Feng, Apl Materials **2**, 081801 (2014).

[74] N. Mounet, Masters Thesis, MIT (2005).

[75] N. L. Vočadlo and G. D. Price, Phys. Earth Planet. Inter. **82**, 261 (1994).

[76] M. Lazzeri and F. Mauri, Phys. Rev. Lett **90**, 036401 (2003).

[77] C. J. Fennie and K. M. Rabe, Phys. Rev. B **68**, 184111 (2003).

[78] V. L. Deringer, R. P. Stoffel, and R. Dronskowski, Phys. Rev. B **89**, 094303 (2014), URL `https://link.aps.org/doi/10.1103/PhysRevB.89.094303`.

[79] C. Ge, M. Hu, P. Wu, Q. Tan, Z. Chen, Y. Wang, J. Shi, and J. Feng, J. Phy. Chem. C **122**, 15973 (2018).

[80] R. Heiderhoff, T. Haeger, N. Pourdavoud, T. Hu, M. Al-Khafaji, A. Mayer, Y. Chen, H.-C. Scheer, and T. Riedl, J. Phys. Chem. C **121**, 28306 (2017).

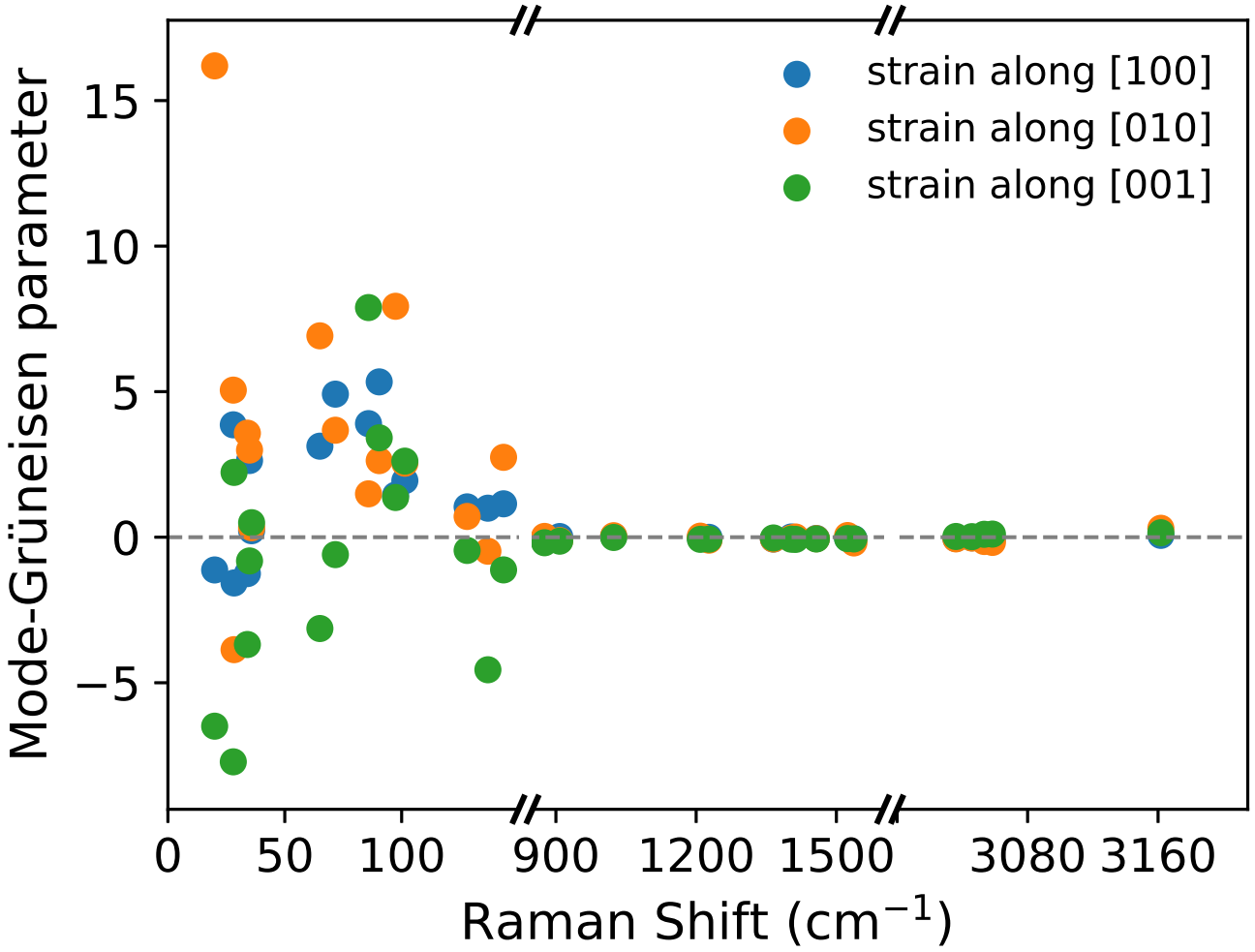

FIG. 11: Calculated mode Grüneisen parameters using slopes of the frequency vs strain graph for each mode in three different crystallographic directions.